

Article

A Comparative Study of Gold Impregnation Methods for Obtaining Metal/Semiconductor Nanophotocatalysts: Direct Turkevich, Inverse Turkevich, and Progressive Heating Methods

Mayra Matamoros-Ambrocio ¹, María de Lourdes Ruiz-Peralta ¹, Ernesto Chigo-Anota ¹ ,
Jesús García-Serrano ², Armando Pérez-Centeno ³, Manuel Sánchez-Cantú ¹,
Efraín Rubio-Rosas ⁴ and Alejandro Escobedo-Morales ^{1,*} 

¹ Facultad de Ingeniería Química, Benemérita Universidad Autónoma de Puebla, C.P. 72570 Puebla, Pue., Mexico; true_may.21@live.com.mx (M.M.-A.); lourdes.ruiz@correo.buap.mx (M.d.L.R.-P.); echigoa@yahoo.es (E.C.-A.); manuel.sanchez@correo.buap.mx (M.S.-C.)

² Centro de Investigaciones en Materiales y Metalurgia, Universidad Autónoma del Estado de Hidalgo, Carretera Pachuca Tulancingo Km 4.5, C.P. 42184 Pachuca, Hidalgo, Mexico; jserrano@uaeh.edu.mx

³ Departamento de Física, CUCEI, Universidad de Guadalajara, Blvd. M. García Barragán #1421, C.P. 44430 Guadalajara, Jalisco, Mexico; armando.centeno@cucei.udg.mx

⁴ Centro Universitario de Vinculación y Transferencia de Tecnología, Benemérita Universidad Autónoma de Puebla, C.P. 72570 Puebla, Pue., Mexico; efrain.rubio@correo.buap.mx

* Correspondence: alejandro.escobedo@correo.buap.mx; Tel.: +52-222-229-5500 (ext. 7250)

Received: 21 March 2018; Accepted: 16 April 2018; Published: 18 April 2018



Abstract: ZnO nanostructures decorated with gold nanoparticles (Au-NPs) were synthesized by thermal decomposition of ZnO₂ powders and their subsequent impregnation of metal nanoparticles using either the Direct Turkevich Method, the Inverse Turkevich Method, or the Progressive Heating Method. It was found that the impregnation approach influences the resulting microstructure and photocatalytic activity of the obtained materials. While the Direct Turkevich approach gave the highest yield of metal loading, the smallest Au-NPs were obtained by Inverse Turkevich and the Progressive Heating Method. The photocatalytic activity of the pristine support and gold-loaded samples was studied in the decolorization of Rhodamine B solutions using UV- and pure visible-light illumination. All Au-NPs/ZnO samples showed higher photocatalytic activity than the bare support when UV-light was used. This effect is attributed to a charge carrier separation due to electron transfer from ZnO to the metal nanoparticles and the built-in electric field at the interfaces. Contrarily to most reports, visible-light sensitization using plasmonic nanoparticles was not observed. The experimental evidence points against hot-electron injection from Au-NPs to the semiconductor component. This behavior is associated with the height of the Schottky barrier at the metal-semiconductor junctions. The differences in the photocatalytic performance among the samples under UV- and visible-light are explained in terms of the characteristics of the Au-NPs driven by the growth mechanism involved in each impregnation method and the physicochemical properties of the generated interfaces.

Keywords: photocatalysis; nanocomposites; metal-semiconductor interface; impregnation method; gold nanoparticles

1. Introduction

During the last decades, the water demand associated with anthropogenic activities has increased notoriously. At the same time, the concentration and diversity of pollutants contained in wastewaters have reached alarming levels. This situation is compromising the potable water availability worldwide; thus, the development of wastewater treatment technologies capable of handling large volumes at lower time and cost has become a priority. In this regard, heterogeneous photocatalysis using semiconductor compounds has proven to be an efficient approach for eliminating recalcitrant pollutants that cannot be removed by other physical, chemical, or biological methods [1–3]. Among the most extensively studied photocatalytic semiconductor compounds is zinc oxide (ZnO). This is mainly because the redox potentials to produce $O_2^{\bullet-}$ and OH^{\bullet} radicals lie between its valence and conduction bands levels [4]. Nevertheless, due to its large band gap energy (~ 3.3 eV), only a limited fraction of sun-light can be used to activate it. In general, two different approaches have been explored to overcome this difficulty: (1) modifying the overall composition to introduce allowed states in the forbidden band gap (doping) or even reduce it (solid solutions); and (2) generating heterojunctions with a visible light-harvesting component (e.g., quantum-dots, plasmonic nanoparticles, narrow band gap semiconductors, or dyes) [5,6]. In this sense, a notorious increase of the photocatalytic activity of ZnO structures by decorating its surface with gold nanoparticles (Au-NPs) has been reported widely [7,8]. Under ultraviolet (UV) illumination, this effect is attributed to an enhanced charge carrier separation due to electron transfer from the ZnO support to Au-NPs, as well as to the built-in electric field generated at the metal-semiconductor interface (Schottky junction) [9,10]. Similarly, when white-light sources (e.g., Xe lamps) are used, again, better performances of the decorated catalysts than their bare counterparts have been observed. However, in this case, and regardless of the fact that the height of the potential barrier at the interface might impede the electron injection [11], the enhancement is commonly attributed to electron transfer from Au-NPs to the semiconductor component [12–15]. Careful revision of the typical experimental set-ups using white-light sources suggests the possibility that the observed photocatalytic activity can be associated merely with a non-filtered UV-light instead of visible light sensitization [16–18]. Moreover, the assignment of electron tunneling as the actual photocatalytic mechanism in Au-NPs/ZnO systems under unfiltered white-light is even more questionable [19–21]. Simply put, the absence of the emission spectrum of the light source does not allow one to assess the photocatalytic mechanism unambiguously.

Although metal-semiconductor photocatalysts based in plasmonic nanoparticles have proven to be potential materials for the development of water treatment technologies, their fabrication methods should attain several attributes prior to being considered in large scale applications. For example, they should produce materials with controlled morphology and large specific surface area; the optical properties of the plasmonic nanoparticles can be tuned to maximize the absorption of the incident light, and a negligible amount of unintegrated metallic phase must result. In this sense, several methods for obtaining photocatalytic nanostructures have been reported [22], and frequently, through a second step, they are decorated with metallic nanoparticles using the well-known Turkevich method [23,24]. As expected, the studies concerning these metal-semiconductor systems demonstrate that their photocatalytic activity is strongly influenced by the characteristic of the metal nanoparticles, e.g., amount, particle size distribution (PSD), morphology, etc. [25–29]. Although the effect to introduce variations in the standard Turkevich protocol in the properties of gold colloids has been extensively explored [30], analogous studies describing the effect of the nucleation sites introduced by an additional interface (support-reaction medium) have not been systematically studied. Specifically, since the growth mechanism of Au-NPs, and thus, their characteristics, could be strongly influenced by the number and kind of interfaces, as well as slight changes in the synthesis protocol, the availability of information concerning their effect should contribute to tuning the actual methods for obtaining metal-semiconductor catalysts with controlled properties.

In this sense, the aim of this work is to study the effect of the impregnation method, namely, Direct Turkevich (standard method), Inverse Turkevich, and the Progressive Heating Method, in the

photocatalytic activity of metal-semiconductor photocatalysts based in ZnO supports decorated with Au-NPs, the latter in terms of the characteristics of the metallic component and its performance in the degradation of Rhodamine B (RhB) solutions under UV- and pure visible-light illumination.

2. Results and Discussion

2.1. Microstructure and Optical Properties

Figure 1 shows photographs of the synthesized ZnO support, Au-NPs/ZnO samples, and the supernatant obtained after gold loading using each impregnation method.

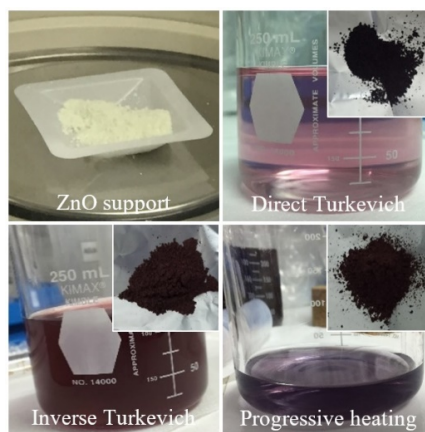


Figure 1. Photographs of the ZnO powder used as photocatalytic support and the supernatant obtained after gold loading using each impregnation method. *Insets:* Obtained Au-NPs/ZnO powders.

The X-ray diffraction (XRD) patterns of the support and Au-NPs/ZnO samples are shown in Figure 2. In the case of the pristine support, all the diffraction peaks correspond to wurtzite zinc oxide (*w*-ZnO; JCPDS # 36-1451); no additional reflection associated with a minority phase was detected. Using the Scherrer equation [31], the average crystallite size of the *w*-ZnO phase was determined to be ~17 nm. The X-ray reflections associated with *w*-ZnO appear also in the patterns of the three gold-loaded samples. However, neither peak broadening nor diffraction angle shift was observed. This indicates that the methods used for metal loading do not induce any significant change in the microstructure of the ZnO support. As can be noted, several X-ray peaks corresponding to cubic gold (*c*-Au; JCPDS # 04-0784) appear in the diffractograms of the three Au-NPs/ZnO samples. The average crystallite size of the *c*-Au phase was estimated to be 12, 9, and 7 nm for the samples obtained using Direct Turkevich Method, Inverse Turkevich Method, and Progressive Heating Method, respectively. It is worth noting that the relative intensity of X-rays associated with *c*-Au phase varies among the samples. This feature indicates that the amount of gold loading depends on the used impregnation method. Qualitatively, the sample obtained using Direct Turkevich Method has the highest gold loading. This result agrees with the chemical analysis and the nearly transparent appearance of the supernatant generated when this method is used (see Figure 1). Table 1 summarizes the intensity ratio of the strongest *c*-Au and *w*-ZnO X-ray peaks, the average crystallite sizes, and the gold content determined by inductively coupled plasma-optical emission spectrometry (ICP-OES) for each sample.

The morphology, particle size, and elemental distribution of the obtained samples were studied using field-emission scanning electron microscopy/energy dispersive X-ray spectroscopy (FE-SEM/EDS) and transmission electron microscopy (TEM). Figure 3a shows a FE-SEM micrograph of the pristine ZnO sample. It reveals that the support is constituted by agglomerates of quasi-spherical nanoparticles of around 90 nm in diameter. After metal impregnation, the morphology of the catalytic support did not change significantly (see Figure 3b). Moreover, EDS elemental mapping suggests that Au-NPs are homogeneously distributed throughout the support (see Figure 3c). Figure 3d–f presents

representative TEM images of the gold loaded samples and their corresponding histogram of Au-NPs. From them, it can be seen that the ZnO particles observed by FE-SEM are nanostructures formed by aggregates of smaller particles of around 15 nm in size and quasi-spherical Au-NPs attached to them (darker particles). The mean particle size (D_m) of Au-NPs was 11.7 ± 2.4 nm, 10.8 ± 1.6 nm, and 9.7 ± 1.8 nm for Direct Turkevich Method, Inverse Turkevich Method, and Progressive Heating Method, respectively. The trend of D_m agrees with the calculated crystallite size determined by XRD.

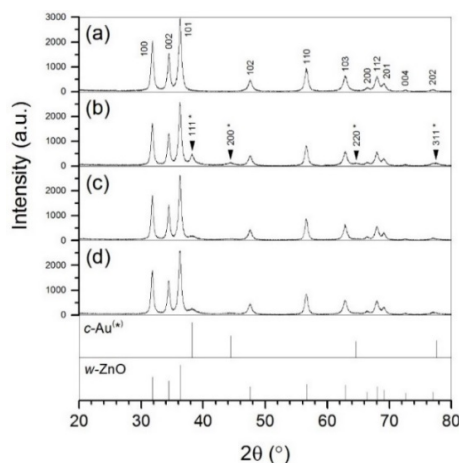


Figure 2. X-ray patterns of (a) the ZnO support and those Au-NPs/ZnO samples obtained using (b) Direct Turkevich; (c) Inverse Turkevich and (d) Progressive Heating as impregnation method. Below: JCPDS # 36-1451 (*w*-ZnO) and JCPDS # 04-0784 (*c*-Au) cards are shown for reference.

Table 1. Intensity ratio of the strongest *c*-Au and *w*-ZnO X-ray reflections [$(I_{111})_{\text{Au}}/(I_{101})_{\text{ZnO}}$], gold loading (Au wt.%), crystallite size (τ), mean particle size of Au-NPs (D_m -Au-NPs), wavelength at the maximum absorbance of the surface plasmon resonance band (SPR- λ_{max}), BET surface area (S_{BET}), decolorization efficiency (η), and apparent rate constant (k) of the obtained catalysts.

	ZnO Support	Au-NPs/ZnO Direct Turkevich	Au-NPs/ZnO Inverse Turkevich	Au-NPs/ZnO Progressive Heating
$(I_{111})_{\text{Au}}/(I_{101})_{\text{ZnO}}$ (a.u.)	0.00	0.19	0.07	0.10
Gold loading (Au wt.%)	—	5.3	1.9	3.8
$\tau_{\text{ZnO}}:\tau_{\text{Au}}$ (XRD) (nm:nm)	17:—	18:12	18:9	18:7
D_m -Au-NPs (TEM) (nm)	—	11.7 ± 2.4	10.8 ± 1.6	9.7 ± 1.8
SPR- λ_{max} (nm)	—:—	534	519	518
S_{BET} ($\text{m}^2 \text{g}^{-1}$)	19.9	21.3	24.6	26.7
UV η ($t = 60$ min): k (%: $\times 10^{-3} \text{min}^{-1}$)	56.4:18.8	97.4:101.1	63.3:23.7	99.9:115.9
Vis η ($t = 60$ min): k (%: $\times 10^{-3} \text{min}^{-1}$)	16.7:2.9	11.3:2.4	9.7:1.3	10.3:2.1

The formation of Au-NPs was further confirmed by diffuse reflectance spectroscopy (DRS). Figure 4 presents the diffuse reflectance spectra (shown as absorbance) of the pristine support and the Au-NPs/ZnO samples. The main feature of the spectrum corresponding to the bare support is a sharp absorption edge around 390 nm. It is associated with the band-gap excitation of ZnO. Using the Kubelka-Munk formalism [32], the apparent band gap energy (E_g) for the semiconductor support was determined to be 3.16 eV (392 nm). The same value was obtained for the Au-NPs/ZnO samples, indicating that metal doping of ZnO did not occur. In the case of the Au-NPs loaded samples, although the adsorption-edge associated with the semiconducting constituent is still recognized, their spectra are dominated by a visible band attributed to the surface plasmon resonance (SPR) of Au-NPs. It is worth noting that the profile, position, and intensity of the SPR-band is different for each sample, indicating that the impregnation method determines the characteristics of the metallic phase.

For instance, the sample obtained using Direct Turkevich Method has the strongest visible absorption among the Au-NPs/ZnO samples. It indicates that this method allows the largest metal loading. Specifically, the gold content for this sample is 5.3 wt.%; being 6.0 wt.% the theoretical maximum yield. The latter agrees with XRD results and the appearance of the supernatant obtained after Au-NPs impregnation. Applying similar arguments to the other Au-NPs/ZnO samples, it is concluded that Inverse Turkevich Method gives the lowest gold loading among the Used Impregnation Methods, in correspondence with the previous results.

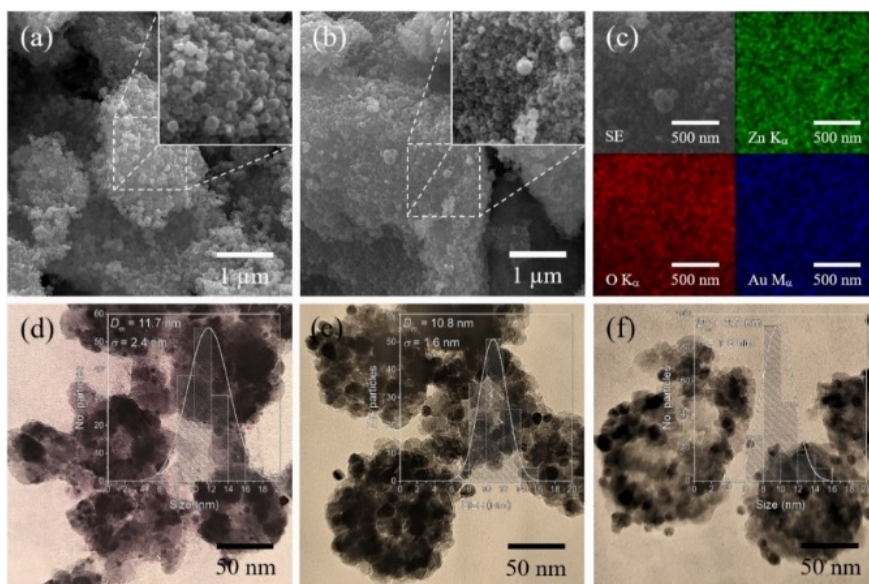


Figure 3. (a) FE-SEM micrograph of the ZnO support, (b) FE-SEM micrograph, and (c) elemental mappings of a representative gold-loaded sample (Progressive heating). TEM images of the samples obtained using (d) Direct Turkevich Method, (e) Inverse Turkevich Method, and (f) Progressive Heating Method and their corresponding particle size histogram of Au-NPs.

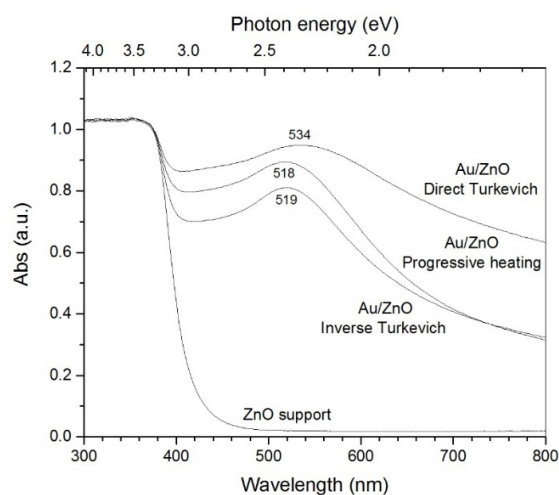


Figure 4. Diffuse reflectance spectra (shown as absorbance) of the ZnO support and those Au-NPs/ZnO samples obtained through different impregnation methods.

Further analysis of the SPR-band gives relevant information related to the PSD of the Au-NPs. While D_m determines the wavelength at the maximum absorbance, the size distribution influences the profile band [33]. From Figure 4, it is seen that the features of the SPR-band of the samples synthesized

using the Inverse Turkevich and Progressive Heating Method are quite similar. This suggests that although both approaches result in different gold loading, the obtained Au-NPs have comparable PSD. On the other side, the SPR-band of the sample obtained by Direct Turkevich Method is considerably broader, and its position is red-shifted by ~ 15 nm ($\lambda_{\max} = 534$ nm). These differences indicate that this approach produces metal nanoparticles bigger in size and with wider PSD than the previous ones. It is worth mentioning that a wide PSD could be an advantageous feature when full range visible light absorption is sought. It is worth noting also that the SPR-band features agree with the TEM particle size analysis described above.

The specific surface area of the different samples was determined using the Brunauer-Emmett-Teller (BET) method. The results are summarized in Table 1. In general, the specific surface area increases after Au-NPs loading. It is attributed to the additional surface accounted by the metal nanoparticles. In this regard, nonetheless, the sample obtained using Direct Turkevich has the highest amount of gold loading, the sample with the largest specific surface area is that synthesized through Progressive Heating Method. It can be understood in terms of the dependence of the surface-volume ratio with particle size. The following rough model illustrates this argument. The specific surface area, S , of a set of solid spheres with particle size distribution, $n(D)$, and density, ρ , is given by

$$S = \frac{6}{\rho} f(D), \quad (1)$$

in which

$$f(D) = \frac{\int_{D_{\min}}^{D_{\max}} D^2 n(D) dD}{\int_{D_{\min}}^{D_{\max}} D^3 n(D) dD} \quad (2)$$

Equations (1) and (2) show that the specific surface area of the spheres is determined by their particle size distribution but not their mass. Moreover, it can be proved that $f(D)$ approaches to $1/D_m$ as the PSD gets narrow and/or the D_m increases. Certainly, our case is more complex; the samples are nanocomposites having Au-NPs as minority phase. Nonetheless, the latter assumption suggests that, at moderate metal loadings, the PSD of metal nanoparticles determines the increase of S rather than their total amount. It is in correspondence with the position of the SPR-band, BET surface area, and gold content of the Au-NPs/ZnO samples (see Table 1).

2.2. Reaction and Growth Mechanism of Au-NPs

The reaction and growth mechanisms of the ZnO nanostructures used as catalytic supports have been described in our previous work [34]. On the other hand, the methods used to decorate them with Au-NPs are variants of those developed by Turkevich et al. in the 1950s [23]. This method is based in the reduction of gold salts using sodium citrate (Na_3Ct), a weak base that acts as stabilizer as well. Two decades later, Frens [24] reported on the effect of $\text{Na}_3\text{Ct}:\text{HAuCl}_4$ ratio in the resulting particle size of Au-NPs. In general, he established that on increasing it, the mean particle size decreases. Nevertheless, Ji et al. [35] found experimental evidence against the validity of this statement at high $\text{Na}_3\text{Ct}:\text{HAuCl}_4$ ratios (>3.5). Moreover, in a series of experiments using equimolar $\text{Na}_3\text{Ct}:\text{HAuCl}_4$ solutions with different concentrations, they demonstrated the role of Na_3Ct as pH mediator and proposed that the preponderant reactive gold species depends on the pH, i.e., the Na_3Ct concentration. In this respect, the highly reactive $[\text{AuCl}_3(\text{OH})]^-$ species is formed at pH's below 6.2, whereas the less reactive species, $[\text{AuCl}_2(\text{OH})_2]^-$ and $[\text{AuCl}(\text{OH})_3]^-$, are favored at higher pH values. Hence, the reaction is faster in the former case. According with these findings, the $\text{Na}_3\text{Ct}:\text{HAuCl}_4$ ratio used in the experiments herein presented (6.8) gave the reaction conditions ($\text{pH} \approx 7.2$) for moderate nucleation and slow growth rates. It agrees with the change in the appearance of the

reaction medium during the experiment using Direct Turkevich method. Since the concentration and $\text{Na}_3\text{Ct}:\text{HAuCl}_4$ ratio were the same in all the impregnation approaches, one would expect that the nucleation and growth rates of Au-NPs were nearly equal. However, the obtained results do not match this assumption. Figure 5 shows the evolution of the appearance of the reaction medium during each impregnation process.

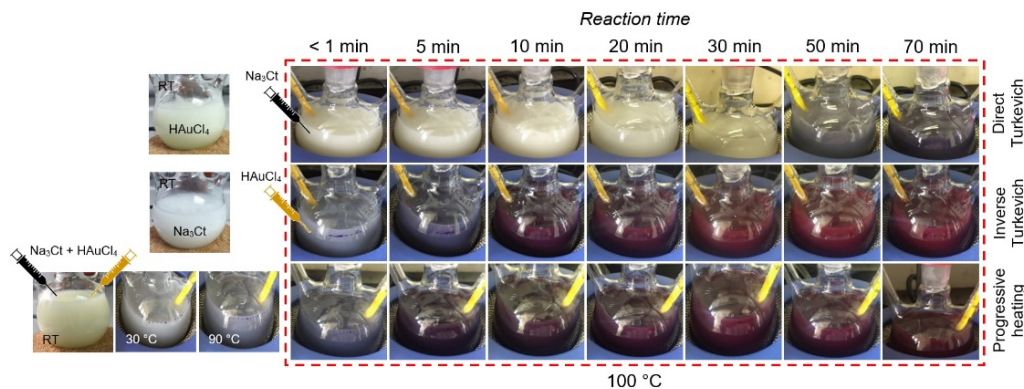


Figure 5. Evolution of the appearance of the reaction medium during the impregnation processes.

As was discussed in the previous section, the sample obtained using Direct Turkevich Method has the broadest PSD of Au-NPs. From Figure 5, it can be noted that the overall transformation rate of Au-NPs using this approach is very slow in comparison with the other two methods. It suggests that, in the case of Direct Turkevich Method, nucleation and growth processes of Au-NPs can occur simultaneously, resulting in a broad PSD. Conversely, nearly instantaneous change is observed in the case of Inverse Turkevich Method and Progressive Heating Method, indicating that high nucleation rates occur, which promote smaller particles with narrow PSD [36].

An analysis of the amount of gold loading achieved by the different impregnation methods reveals further information concerning the growth mechanism. In the case of Direct Turkevich Method, it is 5.3 wt.%, suggesting that most of the Au-NPs form at the solid-liquid interface through heterogeneous nucleation and subsequent growth. It is noticed that the amount of gold loading decreases up to 1.9 and 3.8 wt.% for the Inverse Turkevich Method and Progressive Heating Method, respectively. It follows that, in the former case, a large percentage of Au-NPs remains in the volume of the reaction solution (see Figure 1) instead of the ZnO surface, i.e., homogeneous nucleation dominates over heterogeneous.

Although fundamentally qualitative, the previous analysis demonstrates that the addition order of reagents influences the resulting characteristics of the Au-NPs decorating the surface of the catalytic supports. Ojea et al. [30] have reported an analogous effect in gold colloids. They observed that on reversing the order of reagents in the standard Turkevich protocol (Inverse Turkevich), smaller particles with narrower PSD are obtained. This result was attributed to an increase of the nucleation and growth rate promoted by formation of a strong reducing medium before adding of gold precursor. This medium is generated by the oxidation of Na_3Ct to dicarboxy acetone in heat water, producing chemical intermediates capable of reducing gold species [37]. The same effect seems to apply for our synthesized samples. Thus, it is proposed that the differences in the SPR-band features and gold loading among Au-NPs/ZnO samples can be explained in terms of the growth mechanism for each case. (1) Direct Turkevich Method: The existence of a support-reaction medium interface along with low concentration of reducing species favors heterogeneous nucleation and lead low nucleation rate; thus, bigger Au-NPs with broad PSD are produced [38]; (2) Inverse Turkevich Method: In spite of the nucleation sites at the ZnO surface, the high concentration of reducing species privileges homogeneous nucleation; hence, smaller Au-NPs with narrow PSD result (most as colloid) [39]; however, poor gold loading is achieved; (3) Progressive Heating Method: This method paves the way for intermediate physicochemical conditions in which homogeneous and heterogeneous nucleation compete.

2.3. Photocatalytic Activity

The influence of the impregnation method in the photocatalytic activity of the synthesized samples was studied via their performance in decolorizing RhB solutions under UV- and pure visible-light illumination, using the apparent rate constant k as the comparative parameter. Figure 6 shows the emission spectra of the UV-lamp and sunlight-LED used as light sources. The decolorization curves corresponding to the different photocatalysts are presented in Figure 7.

In agreement with previous reports, under UV illumination, gold loading enhances the photocatalytic performance of the ZnO support. Nonetheless, it is worth noting that the value of k does not increase monotonously with the gold content (Au wt.%) (see Table 1). This behavior has been observed earlier by several authors [40,41], which implies that the catalytic activity of the Au-NPs/ZnO samples is influenced by other aspects of their microstructure. For instance, an increase of the catalytic activity has been reported in metal-semiconductor nanocomposites as the size of the Au-NPs decreases. This effect is attributed to a shifting of the Fermi level towards more negative potentials [25,42]. Additionally, we propose that a greater interaction between the photogenerated charge carriers and the built-in electric field at the metal-semiconductor interfaces contributes to the observed enhancement. To illustrate this idea, consider a set of metal particles with particle size distribution, $n(D)$, and density, ρ . These particles are deposited on a semiconductor surface. The total metal-semiconductor interface area, A_{int} , is then obtained by accounting the interface area formed by each metal particle. Analogously, the total mass of the metallic component, m_T , is obtained by adding the mass of every metal particle. For simplicity, consider hemispherical particles deposited on a flat surface (see inset of Figure 7). In this case, A_{int} is given by

$$A_{\text{int}} = \frac{3m_T}{\rho} f(D) \quad (3)$$

Under this scheme, A_{int} is determined by both PSD and the amount of metal loading. Because the electric fields responsible for the charge carrier separation are located at the Schottky junctions, to extend the A_{int} might increase the interaction probability among it and the photogenerated carriers, reducing the electron-hole recombination rate.

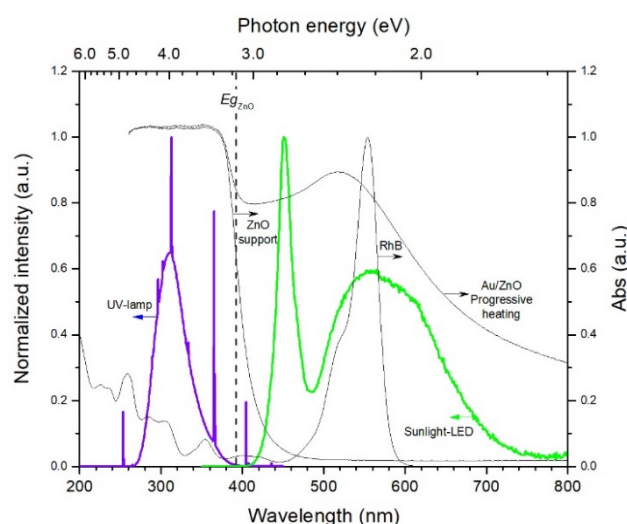


Figure 6. Emission spectra of the UV-lamp and sunlight-LED used as light sources in the photocatalytic experiments. Absorbance spectra of the ZnO support, a representative Au-NPs/ZnO sample, and RhB are shown for comparison.

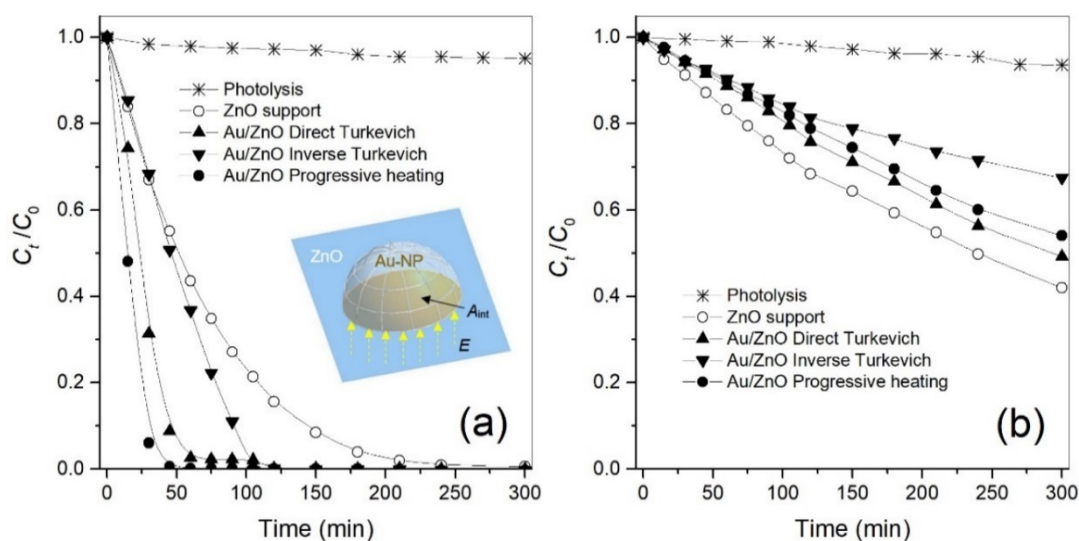


Figure 7. RhB decolorization curves using the synthesized photocatalysts activated by the (a) UV-lamp and (b) sunlight-LED. C_t : RhB concentration at the time t ; C_0 : initial RhB concentration. *Inset*: Scheme of the interface area (A_{int}) formed by deposition of a gold nanoparticle on the ZnO surface.

Based on the previous argument, the differences of the photocatalytic activity among the Au-NPs/ZnO samples can be explained in terms of A_{int} . First, the sample obtained using Progressive Heating Method shows the highest photocatalytic activity. Although this sample has an intermediate gold loading (3.8 wt.%), it has the smallest Au-NPs (~ 9.7 nm) and, in consequence, the largest A_{int} . Second, the sample synthesized using Inverse Turkevich Method shows the lowest photocatalytic activity. This sample has an intermediate Au-NPs size (~ 10.8 nm) but the lowest gold content (1.9 wt.%), resulting in the smallest A_{int} . Third, the sample obtained using Direct Turkevich Method has the largest Au-NPs size (~ 11.7 nm) and the highest gold loading (5.3 wt.%), which compensates the total interface area; thus, an intermediate catalytic performance results.

Contrary to the results discussed above, when pure visible-light is used, all the gold-loaded samples showed less catalytic activity than the bare ZnO support. Under visible-light, the photocatalytic activity of Au-NPs/semiconductor catalysts has been attributed to electron transfer from the plasmonic particles to the conduction band (CB) of the semiconductor support [43]. The injected electrons, called hot-electrons, result from the decay process of excited plasmons. In our samples, since the plasmon energy (~ 2.4 eV) is larger than the interband threshold of gold (~ 2 eV), direct intraband transitions dominates as the plasmon decay mechanism. In gold, the generated hot-electrons and -holes locate at states in the sp -band (~ 0.5 eV above the Fermi level) and d -band (~ 2.5 eV below the Fermi level), respectively [44]. Thus, the injection of hot-electrons into ZnO depends on whether they have enough energy to overcome the Schottky barrier [45]. The value of the potential barrier of Au-ZnO junctions has been reported as large as 1.2 eV [46]. We propose that the Schottky barrier in our Au-NPs/ZnO samples is sufficiently high that hot-electrons are reflected at the metal-semiconductor interfaces. As consequence, gold-loaded samples do not exhibit higher photocatalytic activity than the bare support. In this regard, since the shortest wavelength of the sunlight-LED is still below the ZnO absorption edge (see Figure 6), transfer of photogenerated electrons from the CB of ZnO to the Fermi level of Au-NPs cannot be the involved in the catalytic mechanism. Nevertheless, given that decolorization of RhB solution is yet observed when the bare support is used as catalyst, dye sensitization is proposed as the actual mechanism, i.e., electrons are transferred from the excited RhB molecules (RhB^*) to the CB of ZnO, allowing formation of $O_2^{\bullet-}$ species [47]. However, degradation of organic pollutants is mainly due to OH^{\bullet} radicals produced by water oxidation rather than $O_2^{\bullet-}$ species [48]. In agreement, under pure visible-light illumination, the overall photocatalytic activity of all the samples decreases.

washed with deionized water, and dried at 70 °C for 2 h. The obtained yellowish powder was then placed in an alumina crucible, put at the center of an opened quartz tube, and heated for 2 h at 300 °C; a white ZnO powder was obtained. Gold loading was carried out by following a second step. Briefly, in a three-neck boiling flask fitted with reflux condenser, 600 mg of the ZnO powder was dispersed in 170 mL of deionized water (18.2 MΩ cm) under vigorous magnetic stirring. Previously, two aqueous solutions containing the chemical precursors were prepared: (1) 12.3 mM gold (III) chloride trihydrate (HAuCl₄·3H₂O, ≥99.9%, Sigma-Aldrich, St. Louis, MO, USA) solution (Sol. 1) and (2) 83.6 mM sodium citrate tribasic dihydrate (Na₃Ct; C₆H₅Na₃O₇·2H₂O, ≥99.0%, Sigma-Aldrich) solution (Sol. 2). In all the impregnation protocols, the Na₃Ct:HAuCl₄ molar ratio was fixed at 6.8. This value was selected to set the surface plasmon resonance band of the Au-NPs around 520 nm [30], which lies within the wavelength range with the highest intensity of the terrestrial solar spectrum [51]. In the case of the Au-NPs/ZnO sample obtained through Direct Turkevich Method as impregnation method, first, 15 mL of Sol. 1 was added to the ZnO suspension; then, the reaction temperature was increased to 100 °C. Afterward, 15 mL of Sol. 2 was added, and the reaction temperature was sustained during 70 min. Lastly, the solution was cooled in an ice-bath, and the obtained powder was extracted by centrifugation, washed with distilled water and ethanol, and dried at 70 °C during 2 h. For the sample obtained using Inverse Turkevich Method, merely, the addition sequence of Sol. 1 and Sol. 2 was reversed. In the case of Progressive Heating Method, both Sol. 1 and Sol. 2 were added at the same time before heating the reaction solution.

3.2. Materials Characterization

The obtained samples were characterized by X-ray diffraction (XRD; Advance D8 Discover diffractometer equipped with a Ni-filtered Cu-K_α X-ray tube and a Lynx-Eye detector, Bruker Co., Berlin, Germany), field-emission scanning electron microscopy (FE-SEM; MIRA3-LM FE-SEM, TESCAN, Brno, Czech Republic, operating at 20 kV), transmission electron microscopy (TEM, JEM-2100, JEOL, Tokyo, Japan, operating at 200 kV), elemental mapping using energy dispersive X-ray spectroscopy (EDS; QUANTAX XFlash 6 | 30 EDS detector, Bruker Nano Analytics, Berlin, Germany), diffuse reflectance spectroscopy (DRS; Cary 5000 UV-Vis-NIR spectrophotometer equipped with a DRA-CA-30I accessory, Aligent, Santa Clara, CA, USA), nitrogen adsorption-desorption (BELSORP Mini-II sorptometer, MicrotracBEL Corp., Osaka, Japan; the isotherms were recorded at 77 K, previously, the samples were degassed in vacuum during 5 h at 300 °C), and inductively coupled plasma-optical emission spectrometry (ICP-OES, Optima 8300, Perkin-Elmer, Waltham, MA, USA).

3.3. Photocatalytic Experiments

The photocatalytic activity of the samples was studied by testing their performance in the decolorization of Rhodamine B (RhB; C₂₈H₃₁ClN₂O₃, ~95%, Sigma-Aldrich) solutions irradiated with either UV- or pure visible-light. An UV-lamp (UVP-XX-15S, 302 nm, 15 W) and a sunlight-LED (BLC12W, 5500 K, CRI>83, 12 W) were used as light sources, respectively. Their emission spectra were acquired using a NanoLog[®] spectrofluorometer equipped with a Hamamatsu R-928P photomultiplier tube (Horiba Jobin Yvon Inc. Edison, NJ, USA). The catalytic experiments consisted of dispersing 150 mg of the catalyst in 150 mL of a 5.0 ppm RhB aqueous solution under magnetic stirring. The temperature of the solution was sustained at 20 °C, and 400 sccm of air was bubbled throughout the experiments. Before light irradiation, the dispersion was maintained in dark for 2 h to ensure adsorption-desorption equilibrium. Aliquots were then taken at specific intervals to determine the actual RhB concentration by UV-Vis spectrophotometry (λ_{max} = 553 nm). Analogous experiments, but without dispersing the catalyst, were performed to determine the stability of RhB under illumination (photolysis).

4. Conclusions

ZnO nanostructures were decorated with gold nanoparticles (Au-NPs) using three different approaches, namely, the Direct Turkevich Method, the Inverse Turkevich Method, and the Progressive Heating Method. The photocatalytic activity of the synthesized samples was tested toward decolorization of rhodamine B (RhB) solutions. It was found that the catalytic activity of the Au-NPs/ZnO samples depends on the used impregnation method. It is attributed to differences in the characteristics of the metallic phase driven by the growth mechanism involved in each method. Under UV-light illumination, all the Au-NPs/ZnO samples showed higher catalytic activity than the bare ZnO support. While this effect is associated with a charge carrier separation mechanism, the observed differences among gold-loaded samples are attributed to the total Au-ZnO interface area. Contrary to previous reports, under visible-light, photocatalytic enhancement using Au-NPs was not observed. This result is attributed to the condition that hot-electrons do not have enough energy to overcome the potential barrier at metal-semiconductor interfaces. Therefore, the effectiveness of the visible sensitization using Au-NPs might depend on how much the Schottky barrier is shortened. Finally, it is proposed that under pure visible-light illumination and high Schottky barriers, Au-NPs have a dual role: one as hinder of the dye sensitization mechanism and another as charge-separation promoter.

Acknowledgments: This work was partially supported by the Vicerrectoría de Investigación y Estudios de Posgrado-BUAP (Grant # ESMA-ING18-I). Authors acknowledge U. Pal and A. Méndez Blas for extending the facilities to carry out the nitrogen adsorption-desorption and emission spectra measurements.

Author Contributions: Alejandro Escobedo-Morales conceived and designed the experiments. Mayra Matamoros-Ambrocio, María de Lourdes Ruiz-Peralta and Manuel Sánchez-Cantú synthesized the samples and performed the photocatalysis experiments. Ernesto Chigo-Anota, Jesús García-Serrano, Armando Pérez-Centeno, and Efraín Rubio-Rosas characterized the materials. All the authors contribute to the analysis and discussion of the results, and to the writing of the manuscript.

Conflicts of Interest: The authors declare no conflict of interest.

References

1. Teoh, W.Y.; Scott, J.A.; Amal, R. Progress in Heterogeneous Photocatalysis: From Classical Radical Chemistry to Engineering Nanomaterials and Solar Reactors. *J. Phys. Chem. Lett.* **2012**, *3*, 629–639. [[CrossRef](#)] [[PubMed](#)]
2. Holkar, C.R.; Jadhav, A.J.; Pinjari, D.V.; Mahamuni, N.M.; Pandit, A.B. A critical review on textile wastewater treatments: Possible approaches. *J. Environ. Manag.* **2016**, *182*, 351–366. [[CrossRef](#)] [[PubMed](#)]
3. Fox, M.A.; Dulay, M.T. Heterogeneous photocatalysis. *Chem. Rev.* **1993**, *93*, 341–357. [[CrossRef](#)]
4. Mills, A.; Davies, R.H.; Worsley, D. Water purification by semiconductor photocatalysis. *Chem. Soc. Rev.* **1993**, *22*, 417. [[CrossRef](#)]
5. Reddy, P.A.K.; Reddy, P.V.L.; Kwon, E.; Kim, K.H.; Akter, T.; Kalagara, S. Recent advances in photocatalytic treatment of pollutants in aqueous media. *Environ. Int.* **2016**, *91*, 94–103. [[CrossRef](#)] [[PubMed](#)]
6. Kumar, S.G.; Rao, K.S.R.K. Comparison of modification strategies towards enhanced charge carrier separation and photocatalytic degradation activity of metal oxide semiconductors (TiO₂, WO₃ and ZnO). *Appl. Surf. Sci.* **2017**, *391*, 124–148. [[CrossRef](#)]
7. Mondal, C.; Pal, J.; Ganguly, M.; Sinha, A.K.; Jana, J.; Pal, T. A one pot synthesis of Au–ZnO nanocomposites for plasmon-enhanced sunlight driven photocatalytic activity. *New J. Chem.* **2014**, *38*, 2999. [[CrossRef](#)]
8. Gu, X.; Li, C.; Yuan, S.; Ma, M.; Qiang, Y.; Zhu, J. ZnO based heterojunctions and their application in environmental photocatalysis. *Nanotechnology* **2016**, *27*, 402001. [[CrossRef](#)] [[PubMed](#)]
9. Gerischer, H. A mechanism of electron hole pair separation in illuminated semiconductor particles. *J. Phys. Chem.* **1984**, *88*, 6096–6097. [[CrossRef](#)]
10. Chen, Z.H.; Tang, Y.B.; Liu, C.P.; Leung, Y.H.; Yuan, G.D.; Chen, L.M.; Wang, Y.Q.; Bello, I.; Zapien, J.A.; Zhang, W.J.; et al. Vertically Aligned ZnO Nanorod Arrays Sensitized with Gold Nanoparticles for Schottky Barrier Photovoltaic Cells. *J. Phys. Chem. C* **2009**, *113*, 13433–13437. [[CrossRef](#)]
11. Tung, R.T. The physics and chemistry of the Schottky barrier height. *Appl. Phys. Rev.* **2014**, *1*, 11304. [[CrossRef](#)]

12. Tian, Y.; Tatsuma, T. Plasmon-induced photoelectrochemistry at metal nanoparticles supported on nanoporous TiO₂. *Chem. Commun. (Camb)* **2004**, 1810–1811. [[CrossRef](#)] [[PubMed](#)]
13. Hou, W.; Cronin, S.B. A Review of Surface Plasmon Resonance-Enhanced Photocatalysis. *Adv. Funct. Mater.* **2013**, *23*, 1612–1619. [[CrossRef](#)]
14. Mubeen, S.; Hernandez-Sosa, G.; Moses, D.; Lee, J.; Moskovits, M. Plasmonic Photosensitization of a Wide Band Gap Semiconductor: Converting Plasmons to Charge Carriers. *Nano Lett.* **2011**, *11*, 5548–5552. [[CrossRef](#)] [[PubMed](#)]
15. Zhang, Z.; Li, A.; Cao, S.-W.; Bosman, M.; Li, S.; Xue, C. Direct evidence of plasmon enhancement on photocatalytic hydrogen generation over Au/Pt-decorated TiO₂ nanofibers. *Nanoscale* **2014**, *6*, 5217–5222. [[CrossRef](#)] [[PubMed](#)]
16. Liu, X.; Li, Z.; Zhao, W.; Zhao, C.; Yang, J.; Wang, Y. Zinc Oxide nanorod/Au composite arrays and their enhanced photocatalytic properties. *J. Colloid Interface Sci.* **2014**, *432*, 170–175. [[CrossRef](#)] [[PubMed](#)]
17. Han, Z.; Wei, L.; Zhang, Z.; Zhang, X.; Pan, H.; Chen, J. Visible-Light Photocatalytic Application of Hierarchical Au-ZnO Flower-Rod Heterostructures via Surface Plasmon Resonance. *Plasmonics* **2013**, *8*, 1193–1202. [[CrossRef](#)]
18. Hu, J.; You, N.; Yu, Z.; Zhou, G.; Xu, X. Two-dimensional ZnO ultrathin nanosheets decorated with Au nanoparticles for effective photocatalysis. *J. Appl. Phys.* **2016**, *120*, 74301. [[CrossRef](#)]
19. Wu, S.; Chen, Z.; Wang, T.; Ji, X. A facile approach for the fabrication of Au/ZnO-hollow-sphere-monolayer thin films and their photocatalytic properties. *Appl. Surf. Sci.* **2017**, *412*, 69–76. [[CrossRef](#)]
20. Hang, D.-R.; Islam, S.E.; Chen, C.-H.; Sharma, K.H. Full Solution-Processed Synthesis and Mechanisms of a Recyclable and Bifunctional Au/ZnO Plasmonic Platform for Enhanced UV/Vis Photocatalysis and Optical Properties. *Chem. A Eur. J.* **2016**, *22*, 14950–14961. [[CrossRef](#)] [[PubMed](#)]
21. Kim, K.J.; Kreider, P.B.; Chang, C.H.; Park, C.M.; Ahn, H.G. Visible-light-sensitive nanoscale Au-ZnO photocatalysts. *J. Nanoparticle Res.* **2013**, *15*. [[CrossRef](#)]
22. Li, X.; Yu, J.; Jaroniec, M. Hierarchical photocatalysts. *Chem. Soc. Rev.* **2016**, *45*, 2603–2636. [[CrossRef](#)] [[PubMed](#)]
23. Turkevich, J.; Stevenson, P.C.; Hillier, J. A study of the nucleation and growth processes in the synthesis of colloidal gold. *Discuss. Faraday Soc.* **1951**, *11*, 55–75. [[CrossRef](#)]
24. Frens, G. Controlled Nucleation for the Regulation of the Particle Size in Monodisperse Gold Suspensions. *Nat. Phys. Sci.* **1973**, *241*, 20–22. [[CrossRef](#)]
25. Subramanian, V.; Wolf, E.E.; Kamat, P.V. Catalysis with TiO₂/Gold Nanocomposites. Effect of Metal Particle Size on the Fermi Level Equilibration. *J. Am. Chem. Soc.* **2004**, *126*, 4943–4950. [[CrossRef](#)] [[PubMed](#)]
26. DeSario, P.A.; Pietron, J.J.; DeVantier, D.E.; Brintlinger, T.H.; Stroud, R.M.; Rolison, D.R. Plasmonic enhancement of visible-light water splitting with Au-TiO₂ composite aerogels. *Nanoscale* **2013**, *5*, 8073–8083. [[CrossRef](#)] [[PubMed](#)]
27. Lee, J.; Shim, H.S.; Lee, M.; Song, J.K.; Lee, D. Size-controlled electron transfer and photocatalytic activity of ZnO-Au nanoparticle composites. *J. Phys. Chem. Lett.* **2011**, *2*, 2840–2845. [[CrossRef](#)]
28. Qian, K.; Sweeny, B.C.; Johnston-Peck, A.C.; Niu, W.; Graham, J.O.; DuChene, J.S.; Qiu, J.; Wang, Y.-C.; Engelhard, M.H.; Su, D.; et al. Surface Plasmon-Driven Water Reduction: Gold Nanoparticle Size Matters. *J. Am. Chem. Soc.* **2014**, *136*, 9842–9845. [[CrossRef](#)] [[PubMed](#)]
29. Carabineiro, S.A.C.; Machado, B.F.; Bacsá, R.R.; Serp, P.; Dražić, G.; Faria, J.L.; Figueiredo, J.L. Catalytic performance of Au/ZnO nanocatalysts for CO oxidation. *J. Catal.* **2010**, *273*, 191–198. [[CrossRef](#)]
30. Ojea-Jiménez, I.; Bastús, N.G.; Puentes, V. Influence of the Sequence of the Reagents Addition in the Citrate-Mediated Synthesis of Gold Nanoparticles. *J. Phys. Chem. C* **2011**, *115*, 15752–15757. [[CrossRef](#)]
31. Scherrer, P. Bestimmung der Grösse und der inneren Struktur von Kolloidteilchen mittels Röntgenstrahlen [Determination of the size and internal structure of colloidal particles using X-rays]. *Göttinger Nachrichten Math. Phys.* **1918**, *2*, 98–100.
32. Escobedo Morales, A.; Sanchez Mora, E.; Pal, U. Use of diffuse reflectance spectroscopy for optical characterization of un-supported nanostructures. *Rev. Mex. Fis.* **2007**, *53S*, 18–22.
33. Chen, P.; Liedberg, B. Curvature of the Localized Surface Plasmon Resonance Peak. *Anal. Chem.* **2014**, *86*, 7399–7405. [[CrossRef](#)] [[PubMed](#)]

34. Escobedo-Morales, A.; Téllez-Flores, D.; Ruiz Peralta, M.D.L.; Garcia-Serrano, J.; Herrera-González, A.M.; Rubio-Rosas, E.; Sánchez-Mora, E.; Olivares Xometl, O.; De Lourdes, M.; Peralta, R. Green method for producing hierarchically assembled pristine porous ZnO nanoparticles with narrow particle size distribution. *Mater. Chem. Phys.* **2015**, *151*, 282–287. [[CrossRef](#)]
35. Ji, X.; Song, X.; Li, J.; Bai, Y.; Yang, W.; Peng, X. Size Control of Gold Nanocrystals in Citrate Reduction: The Third Role of Citrate. *J. Am. Chem. Soc.* **2007**, *129*, 13939–13948. [[CrossRef](#)] [[PubMed](#)]
36. Granqvist, C.G.; Buhrman, R.A. Size distributions for supported metal catalysts. Coalescence growth versus ostwald ripening. *J. Catal.* **1976**, *42*, 477–479. [[CrossRef](#)]
37. Kumar, S.; Gandhi, K.S.; Kumar, R. Modeling of formation of gold nanoparticles by citrate method. *Ind. Eng. Chem. Res.* **2007**, *46*, 3128–3136. [[CrossRef](#)]
38. Anumol, E.A.; Kundu, P.; Deshpande, P.A.; Madras, G.; Ravishankar, N. New Insights into Selective Heterogeneous Nucleation of Metal Nanoparticles on Oxides by Microwave-Assisted Reduction: Rapid Synthesis of High-Activity Supported Catalysts. *ACS Nano* **2011**, *5*, 8049–8061. [[CrossRef](#)] [[PubMed](#)]
39. Thanh, N.T.K.; Maclean, N.; Mahiddine, S. Mechanisms of Nucleation and Growth of Nanoparticles in Solution. *Chem. Rev.* **2014**, *114*, 7610–7630. [[CrossRef](#)] [[PubMed](#)]
40. Wang, G.; Zhang, W.; Lian, H.; Liu, Q.; Jiang, D.; Wu, T. Effect of Au loading, H₂O and CO concentration on the stability of Au/ZnO catalysts for room-temperature CO oxidation. *React. Kinet. Catal. Lett.* **2002**, *75*, 343–351. [[CrossRef](#)]
41. Donkova, B.; Vasileva, P.; Nihitjanova, D.; Velichkova, N.; Stefanov, P.; Mehandjiev, D. Synthesis, characterization, and catalytic application of Au/ZnO nanocomposites prepared by coprecipitation. *J. Mater. Sci.* **2011**, *46*, 7134–7143. [[CrossRef](#)]
42. She, P.; Xu, K.; Zeng, S.; He, Q.; Sun, H.; Liu, Z. Investigating the size effect of Au nanospheres on the photocatalytic activity of Au-modified ZnO nanorods. *J. Colloid Interface Sci.* **2017**, *499*, 76–82. [[CrossRef](#)] [[PubMed](#)]
43. Yu, Y.; Wen, W.; Qian, X.-Y.; Liu, J.-B.; Wu, J.-M. UV and visible light photocatalytic activity of Au/TiO₂ nanoforests with Anatase/Rutile phase junctions and controlled Au locations. *Sci. Rep.* **2017**, *7*, 41253. [[CrossRef](#)] [[PubMed](#)]
44. Narang, P.; Sundararaman, R.; Atwater, H.A. Plasmonic hot carrier dynamics in solid-state and chemical systems for energy conversion. *Nanophotonics* **2016**, *5*, 96–111. [[CrossRef](#)]
45. Christopher, P.; Moskovits, M. Hot Charge Carrier Transmission from Plasmonic Nanostructures. *Annu. Rev. Phys. Chem.* **2017**, *68*, 379–398. [[CrossRef](#)] [[PubMed](#)]
46. Brillson, L.J.; Lu, Y. ZnO Schottky barriers and Ohmic contacts. *J. Appl. Phys.* **2011**, *109*, 121301. [[CrossRef](#)]
47. Rochkind, M.; Pasternak, S.; Paz, Y. Using dyes for evaluating photocatalytic properties: A critical review. *Molecules* **2015**, *20*, 88–110. [[CrossRef](#)] [[PubMed](#)]
48. Ishibashi, K.; Fujishima, A.; Watanabe, T.; Hashimoto, K. Quantum yields of active oxidative species formed on TiO₂ photocatalyst. *J. Photochem. Photobiol. A Chem.* **2000**, *134*, 139–142. [[CrossRef](#)]
49. Patil, S.S.; Mali, M.G.; Tamboli, M.S.; Patil, D.R.; Kulkarni, M.V.; Yoon, H.; Kim, H.; Al-Deyab, S.S.; Yoon, S.S.; Kolekar, S.S.; et al. Green approach for hierarchical nanostructured Ag-ZnO and their photocatalytic performance under sunlight. *Catal. Today* **2016**, *260*, 126–134. [[CrossRef](#)]
50. Sarkar, S.; Makhil, A.; Bora, T.; Baruah, S.; Dutta, J.; Pal, S.K. Photosensitive excited state dynamics in ZnO–Au nanocomposites and their implications in photocatalysis and dye-sensitized solar cells. *Phys. Chem. Chem. Phys.* **2011**, *13*, 12488–12496. [[CrossRef](#)] [[PubMed](#)]
51. Chu, S.X.; Liu, L.H. Analysis of terrestrial solar radiation exergy. *Sol. Energy* **2009**, *83*, 1390–1404. [[CrossRef](#)]

